Check for updates

High Power Laser Science and Engineering, (2025), Vol. 13, e56, 12 pages.
doi:10.1017/hpl.2025.36

HIGH POWER LASER SCIENCE AND ENGINEERING

RESEARCH ARTICLE

A platform for all-optical Thomson/Compton scattering with versatile parameters

Siyu Chen[1], Wenchao Yan[1,3], Mingyang Zhu[1], Yaojun Li[1], Xichen Hu[1], Hao Xu[1], Weijun Zhou[1], Guangwei Lu[1], Mingxuan Wei[1], Lin Lu[1,3], Xulei Ge[1,2,3], Boyuan Li[1,3], Xiaohui Yuan[1,3], Feng Liu[1,3], Min Chen[1,3], Liming Chen[1,3], and Jie Zhang[1,2,3]

[1]*State Key Laboratory of Dark Matter Physics, Key Laboratory for Laser Plasmas (MoE), School of Physics and Astronomy, Shanghai Jiao Tong University, Shanghai, China*

[2]*Tsung-Dao Lee Institute, Shanghai Jiao Tong University, Shanghai, China*

[3]*Collaborative Innovation Center of IFSA, Shanghai Jiao Tong University, Shanghai, China*

(Received 14 March 2025; revised 7 April 2025; accepted 16 April 2025)

Abstract

A dual-beam platform is developed for all-optical Thomson/Compton scattering, with versatile parameter tuning capabilities including electron energy, radiation energy, radiation polarization, etc. By integrating this platform with a 200 TW Ti:sapphire laser system, we demonstrate the generation of inverse Compton scattering X-/gamma-rays with tunable energies ranging from tens of keV to MeV. The polarization of X-/gamma-rays is manipulated by adjusting the polarization of the scattering laser. In the near future, by combining this platform with multi-PW laser facilities, our goal is to explore the transition from nonlinear Thomson scattering to nonlinear Compton scattering, ultimately verifying theories related to strong-field quantum electrodynamics effects induced by extreme scattering.

Keywords: inverse Compton scattering; platform; strong-field quantum electrodynamics; X-/gamma-ray

1. Introduction

The investigation of strong-field quantum electrodynamics (SF-QED) processes requires extreme field intensities approaching the Schwinger limit[1], which cannot be reached by state-of-the-art laser facilities. However, when a relativistic electron travels through an existing intense laser field, the field experienced by the electron in its rest frame is Lorentz transformed to a level where SF-QED effects matter. Therefore, relativistic electrons can act as probes to test these effects. This interaction is known as Thomson or Compton scattering, depending on whether the process is elastic or inelastic scattering. During the scattering, collimated X-/gamma-rays are generated and can be used as radiation sources, commonly known as the inverse Compton scattering (ICS) source. Previously, scattering experiments were conducted in the laboratories of particle accelerators, but the remarkable advances in laser wakefield acceleration (LWFA)[2] have now enabled the study of these experiments under the all-optical setup within high-intensity laser laboratories. The principle of the scattering process is shown in Figure 1.

There are two possible configurations for all-optical scattering experiments. One is a simplified version that involves only one laser beam. This laser beam first drives a wakefield accelerator, and then its leftover energy is reflected by a plasma mirror[3–10] onto electrons, causing head-on scattering. The other scheme features a layout with two independently tunable laser pulses[5,11–18]. Although precise temporal and spatial synchronization between the two beamlines is technically difficult, the dual-beam scheme offers the distinct advantage of independently controlling the properties of the scattering process. Each of the two lasers can be individually tuned to optimal conditions, enabling the generation of high-energy electrons and a scattering laser that meets specific requirements, respectively. Specifically, by keeping the parameters of the LWFA constant, one can exclusively manipulate the colliding pulse, enabling a single-variable investigation into the scattering process.

To investigate these scattering processes, we established an experimental platform for dual-beam all-optical Thomson/Compton scattering (EPATCS) with versatile parameter tuning capabilities. The EPATCS is a tabletop electron–photon interaction setup, where high-energy electrons are

Correspondence to: W. Yan, State Key Laboratory of Dark Matter Physics, Key Laboratory for Laser Plasmas (MoE), School of Physics and Astronomy, Shanghai Jiao Tong University, Shanghai 200240, China. Email: wenchaoyan@sjtu.edu.cn

© The Author(s), 2025. Published by Cambridge University Press in association with Chinese Laser Press. This is an Open Access article, distributed under the terms of the Creative Commons Attribution licence (https://creativecommons.org/licenses/by/4.0), which permits unrestricted re-use, distribution and reproduction, provided the original article is properly cited.

https://doi.org/10.1017/hpl.2025.36 Published online by Cambridge University Press

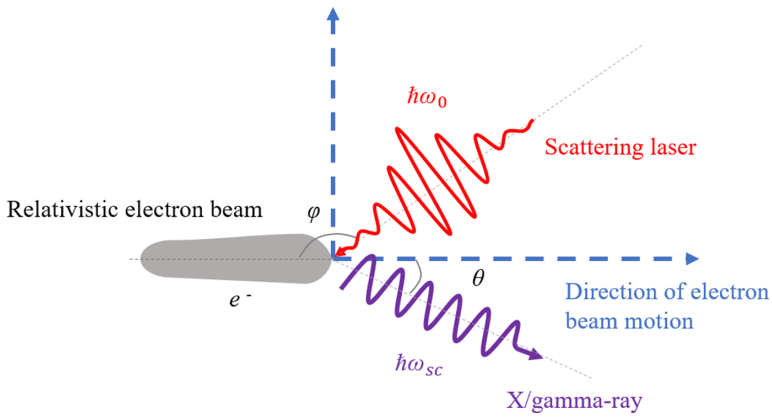


Figure 1. Schematic diagram of the Thomson/Compton scattering process. A relativistic electron beam collides with a scattering laser. The electrons oscillate and emit X-/gamma-rays. Here, φ denotes the collision angle between the laser and the electron beam, θ represents the radiation observation angle, ω_0 signifies the central frequency of the scattering laser photon and ω_{sc} corresponds to the frequency of the emitted photon.

accelerated by one laser beam and then collide with the second laser beam. The flexibility in parameter tuning not only enhances control over experimental conditions, but also opens up new prospects for investigating high-field scattering processes. By precisely controlling the intensity, polarization state and field mode of the colliding laser beam, we can generate X-/gamma-rays with varying characteristics, which can serve as light sources for applications such as high-density dynamic imaging[19–26] and vortex photons for photonuclear physics[27,28]. The EPATCS can also be built on PW laser facilities and provides the possibility of interaction between multi-GeV electrons and high laser intensity under extreme conditions[18] to study SF-QED effects, including the radiation reaction[11,12], pair production[10,29–31], conversion of angular momentum transfer in the collision process[32–34], etc.

This paper is organized as follows. In Section 2, we discuss the versatile tuning of ICS X-/gamma-ray source parameters and their impact on enhancing control over high-field processes and tunable radiation spectra. Section 3 presents the experimental results based on the EPATCS at the 200 TW laser of Shanghai Jiao Tong University. In Section 4, we elucidate the prospective SF-QED research of the EPATCS.

2. Versatile tuning parameters of the experimental platform for dual-beam all-optical Thomson/Compton scattering

The EPATCS offers the potential for multi-parameter adjustments, including tuning the electron beam energy, altering the collision angle between electrons and photons and adjusting the parameters of the colliding laser (such as the laser intensity, wavelength, polarization and orbital angular momentum). In this section, we introduce the experimental designs and explorations to investigate the adjustable parameters and their effects on radiation.

A schematic diagram of a dual-beam collision layout is as shown in Figure 2(a), to investigate the influence of multiple parameters on the photon energy of radiation in the ICS process. The combination of the optical system and guide rail enables precise adjustments to the electron–laser collision angle. Adjustments in the collision angle φ, the focusing intensity a_0, the wavelength λ, the polarization state P and the orbital angular momentum $\vec{L}$ of the colliding beam will significantly alter the characteristics of the radiation emitted. Adjusting the collision angle φ results in a significant variation in the energy spectrum of the X-/gamma-ray from tens of keV to MeV[35]. When the normalized vector potential of the colliding laser, a_0, varies from less than 1 to greater than 1, the electron–photon interaction shifts from a linear to a nonlinear process[13,16,17]. Modifying the wavelength λ alters the colliding laser photon energy $E_0 = \hbar c/\lambda$, which in turn modifies the energy of the scattered photons, that is, the radiation energy[15]. Since this is a fundamental model of the scattering process, the polarization state of the colliding laser directly influences the polarization of the emitted radiation[9]. When the colliding laser is transformed from a Gaussian laser to a Laguerre–Gaussian laser, adjustments in the orbital angular momentum directly affect the orbital angular momentum of the X/gamma radiation[32,36].

To illustrate this principle with a specific example, adjusting the collision angle demonstrates how changes in laser parameters can regulate radiation. In the ICS process, altering the collision angle between electrons and photons can significantly modify the energy spectrum of the emitted radiation. The energy of the emitted photon E_{sc} can be expressed by the following[37]:

$$E_{sc} = E_0 \frac{2n\gamma_e^2 (1-\cos\varphi)}{1 + a_0^2/2 + \gamma_e^2\theta^2}, \quad (1)$$

https://doi.org/10.1017/hpl.2025.36 Published online by Cambridge University Press

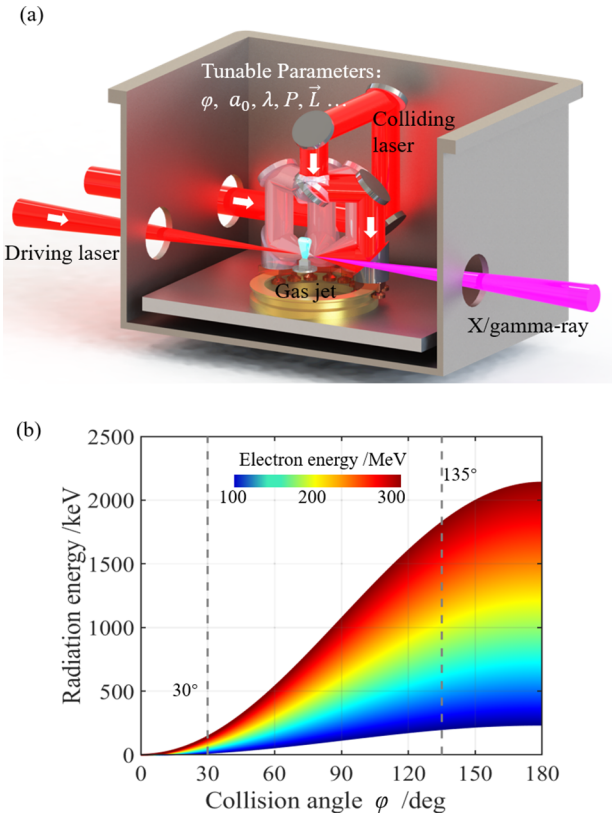


Figure 2. (a) Schematic diagram of the experimental layout with multiple collision angles. (b) Radiation energy under different collision angles φ with electron energy from 100 MeV (blue) to 300 MeV (red) when the observed angle $\theta = 0°$. The cases of 30° and 135° are specifically marked to correspond with the experimental results discussed later in Section 3.2.

where n represents the nonlinear order, E_0 represents the incident photon energy, γ_e denotes the Lorentz factor of an electron, $a_0 = eA_0/m_e c$ is the normalized amplitude of the vector potential and e and m_e are the elementary charge and the rest mass of the electron, respectively. According to Equation (1), the energy of the scattered photons is correlated with that of the incident photons in the following manner: $E_{sc} \sim E_0 \gamma_e^2 \eta$, where $\eta = 1 - \cos\varphi$ is a parameter related to the collision angle, exhibiting a clear range from 0 to 1. Therefore, altering the collision angle acts as an effective approach to enable the continuous adjustment of the ICS radiation energy range. Figure 2(b) illustrates the radiation energy at the observation angle of $\theta = 0°$ generated by linear ICS at various collision angles for electron energies ranging from 100 to 300 MeV.

In Section 3, the collision angle φ and the polarization state of the colliding laser are altered to validate the feasibility of this platform. In Section 3.2, the ICS processes are experimentally validated at collision angles of 30° and 135°, corresponding to the theoretical values calculated in Figure 2(b), and the corresponding radiation energy spectra are diagnosed and analyzed.

3. X-/gamma-ray manipulation by the experimental platform for dual-beam all-optical Thomson/Compton scattering on a 200 TW laser

To validate the applicability of the EPATCS, it was initially integrated into the 200 TW Ti:sapphire laser facility at the Key Laboratory for Laser Plasmas of Shanghai Jiao Tong University. A 5 J p-polarized laser pulse with a duration of $\tau = 25$ fs (full width at half maximum, FWHM) can be delivered to the target. A schematic diagram of the experimental setup and its primary components are referenced in Appendix B.

3.1. Energy tunability of X-/gamma-rays via LWFA electrons

The laser pulse for LWFA is focused by an off-axis parabolic (OAP) mirror of $F\#$ 20 to a Gaussian-like spot size, containing 30% energy with an FWHM diameter of 26 μm, and the focused laser intensity can reach up to 5×10^{18} W · cm^{-2}, corresponding to a normalized vector potential of $a_0 = 2$. The laser was focused above a supersonic gas jet of nitrogen. The electron energy can be effectively adjusted by modifying the relative position of the nozzle and the laser focus and adjusting the plasma density.

As shown in Figure 3, consistent energy electron beams, tunable within the range of 200–600 MeV, can be achieved under stable conditions. For each scenario, the plasma density and acceleration length are indicated, resulting in relatively stable electron energy spectra. Under appropriate plasma density, decreasing the acceleration length within a certain range can effectively enhance the energy of relativistic electrons. The corresponding electron spectrum is shown in Figures 3(a)–3(d). However, as shown in Figures 3(d) and 3(e), when the plasma density is significantly increased, the phase velocity of the wakefield decreases, causing the electrons to dephase earlier, leading to a reduction in their energy. Based on the scale shown in Figure 3 and the actual distance of the image plate from the target, which is 1.6 m, the transverse divergence angle of the electron bunch is approximately 3 mrad (FWHM).

The tuning energy of the electron enables the radiation energy spectrum to span a wide range. As indicated in Equation (1), when $a_0 \ll 1$ (linear scattering regime), the energy of the emitted photon E_{sc} is directly proportional to the square of the electron Lorentz factor γ_e, a relationship that has been verified in several laboratories[13,16,38]. Figure 2(b) demonstrates that under a fixed collision angle, the radiation energy spectrum varies accordingly with changes in electron energy.

3.2. Energy control of X-/gamma-rays by the interaction angle

In the scattering experiments, the relativistic electrons generated by LWFA have a cut-off energy of approximately

https://doi.org/10.1017/hpl.2025.36 Published online by Cambridge University Press

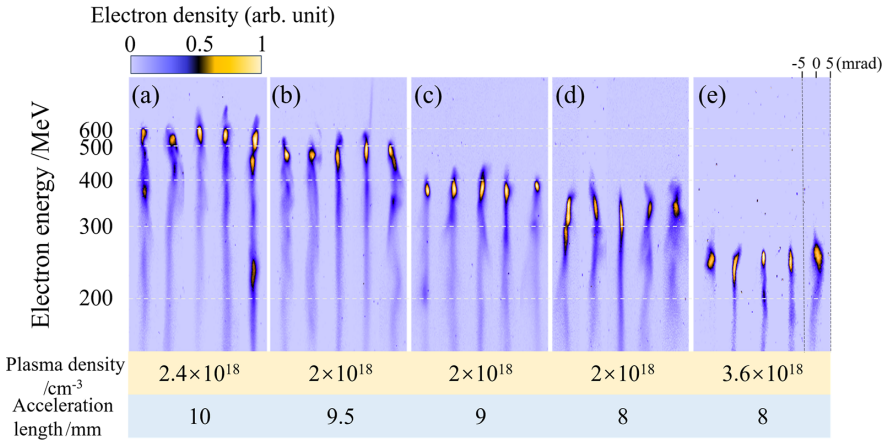


Figure 3. Diagnosis results of the electron beam with different acceleration lengths or plasma densities. From (a) to (e), the corresponding plasma densities are 2.4×10^{18}, 2×10^{18}, 2×10^{18}, 2×10^{18} and 3.6×10^{18} cm^{-3}, respectively, with acceleration lengths of 10, 9.5, 9, 8 and 8 mm.

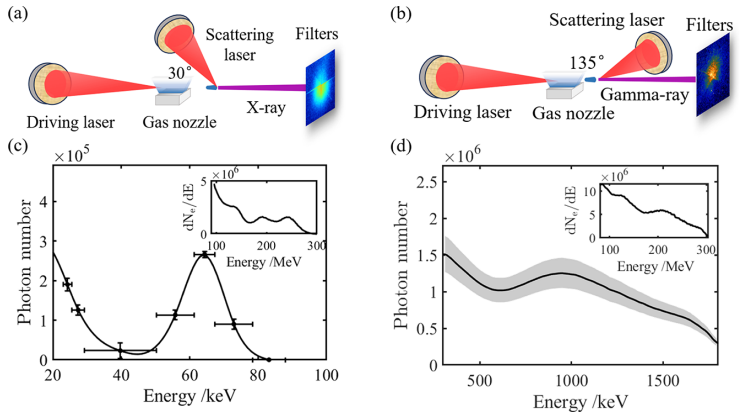


Figure 4. (a), (b) Experimental layout diagrams of AOICS under two conditions of 30° and 135° collision angles, respectively. (c), (d) Radiation spectra with error bars for collision angles of 30° and 135°, respectively. The corresponding electron energy spectrum for each instance is displayed in the upper right-hand corner of each graph.

300 MeV, approaching a continuous spectrum. Two experimental configurations with collision angles of $\varphi = 30°$ and $\varphi = 135°$ are set, as shown in Figures 4(a) and 4(b), respectively. The colliding beam is derived from the main laser pulse using a small pick-up mirror and is focused to a spot with an 8 μm FWHM. With a pulse energy of 200 mJ and a pulse duration of 25 fs, the on-target peak intensity is approximately 4.8×10^{18} $W \cdot cm^{-2}$. The range of the radiation spectrum can be determined by altering the collision angle using Equation (1). Metal filter sheets of various materials and thicknesses are designed for radiation diagnosis.

In the experimental setup with a collision angle of 30°, Ross filter pairs were selected on the basis of the K-absorption edges of metal filters with varying materials and thicknesses. The signal on the image plate behind the filters was obtained from a single shot. Using the least-squares method, we obtained convergence results and derived the energy spectrum. As shown in Figure 4(c), the quasi-monoenergetic peak of the X-ray spectrum at around 65 keV might come from ICS involving only a subset of electrons. When the electron beam interacts with the laser beam at a small angle, their velocities become comparable, causing the laser pulse to continuously interact with the same portion of the electrons within the Rayleigh length. This consequently results in the production of quasi-monochromatic X-rays.

In the case of a collision angle of 135°, the radiation energy spectrum extends beyond 1 MeV. The intensity distribution of the high-resolution CsI fluorescence from a single shot, located behind the filters, was captured by a 16-bit Andor electron-multiplying charge-coupled device. The iterative least-squares method is adopted for the numerical analysis of the transmission coefficient[39] to calculate the final energy spectrum of the X-rays, as illustrated in Figure 4(d). Variations in the collision angle impact the radiation energy spectrum, which is directly influenced by the electron energy spectrum. The basic principles of spectrum diagnostics can be referred to in Appendix A.

https://doi.org/10.1017/hpl.2025.36 Published online by Cambridge University Press

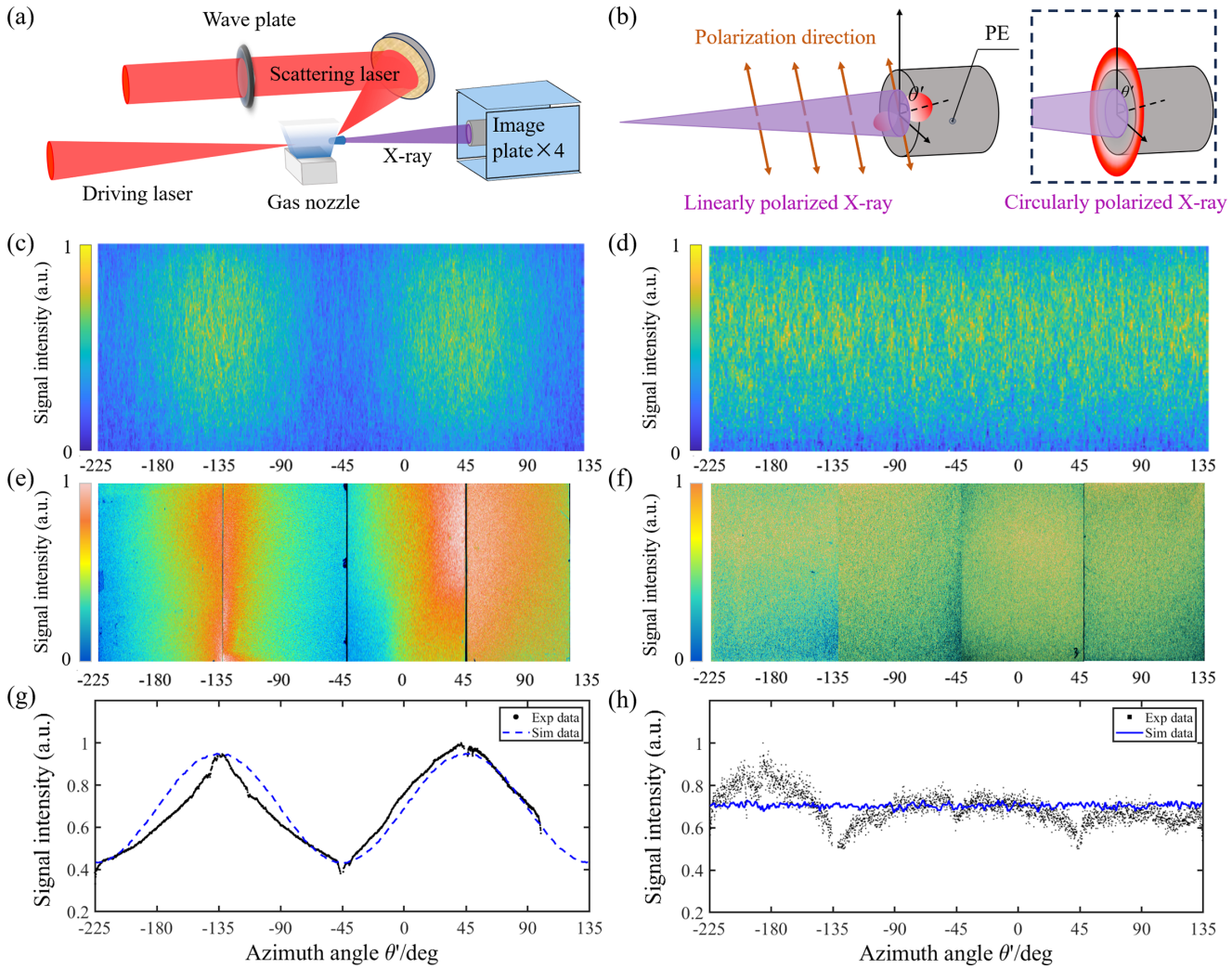


Figure 5. (a) Experimental layout. The polarization state of the X-ray was obtained by placing the polyethylene (PE) forward in the X-ray and placing four image plates around it to diagnose the signal scattering in different polarization states. (b) Schematic representation of Compton scattering of linearly/circularly polarized X-rays with PE scatterers. The red portions indicate the distribution direction of the scattered electrons. (c), (d) Simulation results by FLUKA software, corresponding to the respective Compton scattering signals of linearly polarized and circularly polarized X-rays with PE. (e), (f) Experimental diagnostic results of linearly polarized and circularly polarized X-rays, respectively. (g), (h) The signal image formed by black dots is the one-dimensional integral result of the experimental results, while the dashed blue line represents the simulation results.

3.3. Polarization control of X-/gamma-rays

Polarized X-rays can be used to probe the characteristics of magnetic structures in structural magnetism and distinguish between chiral and helical magnetic structures[40–44]. Based on the EPATCS, we generate polarized X-rays via the collision of a polarized laser beam and the electrons. As shown in Figure 5(a), a half-wave plate or a quarter-wave plate is incorporated into the scattering laser path to change the polarization state of the scattering laser, which in turn modifies the polarization state of the generated radiation. An OAP mirror of *F*# 5 is used to focus the colliding laser. Under linear polarization conditions, the focal spot diameter and laser intensity are the same as those presented in Section 3.2, whereas under circular polarization, the laser intensity is approximately 2.4×10^{18} W·cm^{-2}. The collision angle is 135° and the experimental layout is as illustrated in Figure 5(a).

As shown in Figure 5(a), a cylindrical polyethylene converter with a diameter of 2 cm and a length of 15 cm is placed 1.9 m from the impact point, and four image plates are placed around the converter. The secondary photon signal radiated on the scatterer is diagnosed in the vertical direction of X-ray propagation based on the Compton scattering. When the scattering angle is close to 90°, the azimuth distribution of scattered photons is highly dependent on X-ray polarization, making Compton scattering effective for the diagnosis of polarization[45]. The expressions of the scattering cross-section of Compton scattering in the vertical direction of propagation for linear polarization (see Equation (2)) and

https://doi.org/10.1017/hpl.2025.36 Published online by Cambridge University Press

circular polarization (see Equation (3)) are as follows[46]:

$$\frac{\mathrm{d}\sigma_{\mathrm{lin}\perp}}{\mathrm{d}\Omega} = \frac{1}{4}r_{\mathrm{e}}^2\left(\frac{\varepsilon}{\varepsilon_0}\right)^2\left(\frac{\varepsilon}{\varepsilon_0}+\frac{\varepsilon_0}{\varepsilon}-2\cos^2\theta'\right), \quad (2)$$

$$\frac{\mathrm{d}\sigma_{\mathrm{cir}\perp}}{\mathrm{d}\Omega} = \frac{1}{4}r_{\mathrm{e}}^2\left(\frac{\varepsilon}{\varepsilon_0}\right)^2\left(\frac{\varepsilon}{\varepsilon_0}+\frac{\varepsilon_0}{\varepsilon}\right), \quad (3)$$

where r_{e} represents the classical radius of the electron, where ε_0 is the energy of the incident photon, ε is the energy of the scattered photon and θ' denotes the scattering azimuth angle. According to Equation (2), Compton scattering of linearly polarized X-rays through the scatterer in the vertical direction is a function of the azimuth angle θ'. When the incident X-ray is circularly polarized, Equation (3) reveals that the vertical Compton scattering is independent of the azimuth angle θ'. In the experiment, the optical axis of the half-wave plate is adjusted to an angle of 22.5° from the original horizontal polarization direction, thus producing a linear polarization angle of 45° from the horizontal direction, as shown in Figure 5(b). The reason behind this choice of angle is to facilitate differentiation of the background signal. Due to the wide spectral width of the laser and the bandwidth limitations of the quarter-wave plate, the conversion efficiency of linearly polarized light to circularly polarized light is approximately 80%.

We conducted simulations using FLUKA software to simulate the process; the results are shown in Figures 5(c) and 5(d) and the experimental results are shown in Figures 5(e) and 5(f). Each result accumulated 100 shots, which facilitated the diagnosis of the polarization characteristics of the radiation through the scattered electron distribution. The four image plates are arranged to correspond to azimuth angles ranging from −225° to 135°, with the portion corresponding to 100°–135° being absent, due to constraints on the size of the image plate. Figures 5(g) and 5(h) include both theoretical simulation results and experimental data, with normalized intensity signals. The linear polarization diagnostics show a periodic intensity distribution across the four image plates, indicative of a Compton scattering signal corresponding to the scattering of linearly polarized X-rays. The generated linearly polarized radiation spectrum is illustrated in Figure 4(b). The degree of polarization $(I_{\max}-I_{\min})/(I_{\max}+I_{\min})$ according to the experimental results is about 0.42, and the background greatly influences this result. Moreover, the diagnostic results of circularly polarized X-rays exhibit uniformly distributed intensity signals overall, although a weak periodic intensity distribution signal is still observed near −180°. This suggests that the degree of polarization of circularly polarized X-rays generated by the ICS is not 100%, but rather an elliptical polarization state along the transverse axis. This result matches the effect of the wave-plate bandwidth described above. Our results show that the X-ray diagnostics for circular polarization lack full symmetry. This asymmetry arises from the off-center positioning of the polyethylene scatterer during X-ray irradiation[9].

The aforementioned experimental results demonstrate precise control over electron energy, with a wide range of radiation energy and polarization states. These verify the versatile multiparameter tunability of the EPATCS. In our platform, the pulse duration of the electron bunch generated by LWFA is typically a few femtoseconds[47], and the laser pulse duration is 25 fs. Therefore, in order to realize the collision process described in Sections 3.2 and 3.3, following the approaches outlined in previous works[48,49], we implemented spatial and temporal synchronization, achieved measured time jitters below 10 fs and maintained a high spatial accuracy of electron–photon collisions within 5 μm. Moreover, our experimental results confirm that this level of precision is essential for stable electron–laser collisions.

4. Prospective roadmap for strong-field quantum electrodynamics research via the experimental platform for dual-beam all-optical Thomson/Compton scattering

By integrating with multi-PW laser facilities, the adjustable parameters of the EPATCS provide a fundamental platform for the approaching research initiatives, including multiphoton Thomson/Compton scattering, radiation reaction, vacuum polarization effects and pair production[45,50–55]. When high-energy electrons interact with an intense laser, and the laser intensity in the rest frame of the electron approaches or reaches the Schwinger critical field $E_{\mathrm{s}} = m_{\mathrm{e}}^2c^3/e\hbar$, the relativistic and nonlinear effects of the electrons in the electric field become significant. To describe such quantum effects, the quantum nonlinearity parameter $\chi_{\mathrm{e}} = \sqrt{\left(F^{\mu\nu}p_\mu\right)^2}/(E_{\mathrm{s}}m_{\mathrm{e}}c)$ is defined, where $F^{\mu\nu} = \partial_\mu A_\nu - \partial_\nu A_\mu$ is the four-tensor electromagnetic field and p_μ represents the particle's four-momentum. When $\chi_{\mathrm{e}} \ll 1$, classical electrodynamics can effectively describe the interaction between particles and electromagnetic fields. When $\chi_{\mathrm{e}} \gtrsim 1$, quantum effects (such as electron–positron pair production and nonlinear Compton scattering) become significant, and classical theories are no longer applicable.

We plan to go through a three-phase development process to explore the SF-QED process through the EPATCS. Table 1 presents the fundamental experimental proposal and parameters.

In phase I, the EPATCS will be transferred and built in multiple advanced laser facilities. The platform will be transferred to the 0.5 PW femtosecond laser facility, which is commissioned in the Key Laboratory for Laser Plasmas at Shanghai Jiao Tong University. According to the matching condition of the LWFA, a low-energy dispersive electron beam with a maximum energy of less than 1 GeV can be generated stably. Another focused laser beam with an intensity of up to 10^{21} W·cm^{-2} corresponds to a normalized intensity

https://doi.org/10.1017/hpl.2025.36 Published online by Cambridge University Press

Table 1. The fundamental experimental proposal and parameters.

	Fundamental experimental proposal	Electron energy γ	Normalized intensity a_0	Quantum parameter χ_e
Phase I	From linear to nonlinear regime of ICS; precision experiment of radiation reaction	$\lesssim 2000$	20	$\lesssim 0.2$
Phase II	Research of CRDR for Compton scattering	~ 4000	40–60	~ 1
Phase III	Research of QRDR for Compton scattering and the nonlinear Breit–Wheeler process	$\gtrsim 4000$	~ 200	$\gtrsim 4$

of $a_0 \sim 20$. Under this premise, the quantum parameter is $\chi_e \sim 0.2$. In this regime, electrons interacting with an intense laser field undergo nonlinear Compton scattering, with multiphoton scattering emerging as a significant characteristic. The emission of high-energy radiation results in significant energy loss for the electrons. Future scientific exploration based on this platform will focus on investigating radiation reaction effects, nonlinear Compton scattering, etc.

In phase II, the platform will be transferred to PW-level laser facilities, for instance, on a 1 PW laser facility at the Synergetic Extreme Condition User Facility (SECUF) of the Institute of Physics in the Chinese Academy of Sciences. It can contribute to studies of the classical radiation-dominated regime (CRDR)[54,55] with normalized amplitude $a_0 \sim 40$. It can also be transferred to a 2.5 PW Ti:sapphire femtosecond laser system at the Tsung-Dao Lee Institute (TDLI), with a normalized amplitude a_0 that can be up to 60. Meanwhile, a high-quality electron beam with a central energy of 2 GeV, corresponding to $\gamma \approx 4000$, can be generated using an intense PW laser. At this point, the quantum parameter is $\chi_e \sim 1.4$, which allows the radiation reaction phenomenon to be observed more directly. Independently, high-precision spatiotemporal synchronization of the EPATCS is crucial to validate and explore the locally monochromatic approximation (LMA)[56] and the local-constant-field approximation (LCFA)[57–61]. As the phenomenon becomes more pronounced, it will deepen our understanding of the fundamental principle of SF-QED.

In phase III, the EPATCS could be transferred to 10 PW laser facilities, such as SULF[62], SEL[63], APOLLON[64], ELI[65,66] and EP-OPAL[67]. Considering that a stable electron energy of multi-GeV could be generated, the normalized amplitude a_0 of the scattering laser would be up to 200, when the laser beam is focused to the diffraction limit, and the quantum parameter could be higher than 4. When $a_0 \gtrsim 137$ and $\chi_e \gtrsim 1$, the radiation reaction in each photon emission is generally substantial and is fully accounted for within the context of SF-QED[68,69]. Under such conditions, quantum effects will become consequential, which will be conducive to researching the experimental phenomena in the quantum radiation-dominated regime (QRDR)[54,69,70]. Furthermore, in this scenario, when the electron collides with the laser, the resulting high-energy gamma photons interact again with the intense laser. This interaction allows for effective detection of pair production, providing experimental evidence for the nonlinear Breit–Wheeler process[29,31]. This will deepen our understanding of SF-QED processes and further refine the SF-QED theories and experimental validation. The relevant international experimental progress and proposals are summarized in Figure 6.

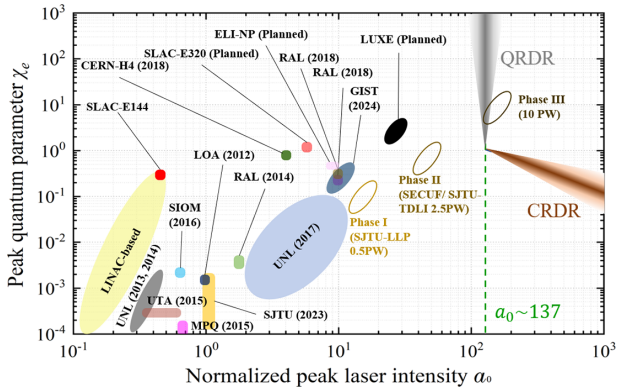


Figure 6. The relevant international experimental progress and proposals[3–6,11–17,71–80]. The solid-colored sections represent experiments that have been completed or are currently being planning, while the hollow elliptical regions correspond to the parameter ranges associated with the three phases discussed in this paper. The ranges corresponding to the classical radiation-dominated regime (CRDR) and the quantum radiation-dominated regime (QRDR) are indicated.

5. Conclusions

The development of an all-optical Thomson/Compton scattering platform, the EPATCS, featuring versatile parameter tunability, harnesses the exceptional benefits of LWFA and super-intense ultrafast lasers. We successfully demonstrate the capability of the EPATCS by providing precise control over the parameters of the X-rays of ICS, including the energy spectrum, polarization state and other parameters of high-energy radiation. With the ongoing development of super-intense ultrafast laser facilities, we aim to explore SF-QED in depth under various physical regimes, including radiation damping, nonlinear Compton scattering and nonlinear Breit–Wheeler electron–positron pair production.

Appendix A. Principle of X-/gamma-ray spectrum diagnostics

Due to differences in X-ray energy resulting from collisions at different angles, two diagnostic approaches are implemented.

https://doi.org/10.1017/hpl.2025.36 Published online by Cambridge University Press

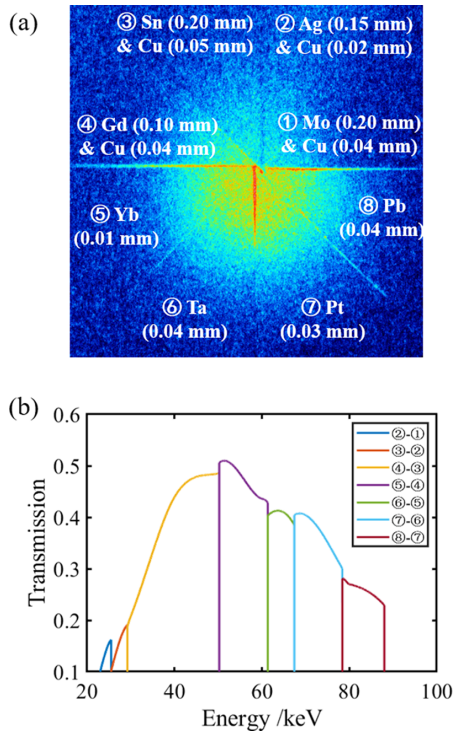


Figure 7. (a) The signal intensity distribution on the image plate in the 30° collision angle ICS experiment, along with the corresponding types of metal filters and their respective thicknesses. (b) The transmission curves for different energy intervals are obtained by subtracting the transmission rates of adjacent filter combinations, where the annotated numbers correspond to the numbers in (a).

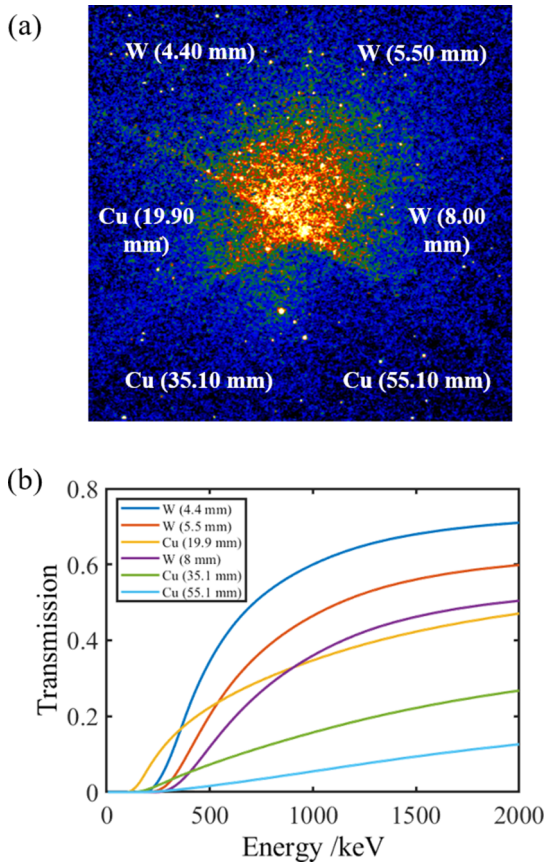


Figure 8. (a) The signal intensity distribution on the image plate in the 135° collision angle ICS experiment, along with the corresponding types of metal filters and their respective thicknesses. (b) The radiation transmittance curves of different metal filters varying with energy.

In the ICS experiment with a collision angle of 30°, the X-ray energy range of 10–100 keV can be predicted based on Equation (1) in the main text and the electron spectrum. Within this energy range, the sector-shaped Ross filter was utilized for spectral diagnostics[81]. The corresponding reference formula is as follows:

$$S_k - S_{k+1} = \int \mathrm{d}(E)\left[T_k(E) - T_{k+1}(E)\right] R(E) \frac{\mathrm{d}N}{\mathrm{d}E}, \qquad (4)$$

where S_k $(k = 1, 2, 3, \dots)$ represents the signal intensity on the imaging plate after X-rays pass through metal filters of different types and thicknesses, T_k $(k = 1, 2, 3, \dots)$ denotes the transmission of the filters for X-rays, $R(E)$ indicates the response efficiency of the imaging plate to X-rays at different energy levels and $\mathrm{d}N/\mathrm{d}E$ describes the final X-ray energy spectrum.

The signal distribution on the image plate behind the filters is shown in Figure 7(a), and the transmission rate subtractions between adjacent filters are shown in Figure 7(b). In the spectral deconvolution calculation, we assume that $\mathrm{d}N/\mathrm{d}E$ is an independent value within each energy interval, thus simplifying Equation (4) to the following:

$$\frac{\mathrm{d}N}{\mathrm{d}E} = \frac{\int \mathrm{d}(E)\left[T_k(E) - T_{k+1}(E)\right] R(E)}{S_k - S_{k+1}}. \qquad (5)$$

By calculating $\mathrm{d}N/\mathrm{d}E$ for different intervals and selecting the midpoint of each interval as the corresponding energy value, the spectrum curve of X-rays can be obtained. The horizontal error originates from the actual range of each energy interval, while the vertical error arises from the intensity fluctuations in the extracted signal region and the measurement error of the image plate response curve[82].

When the collision angle is 135°, the calculated gamma-ray spectrum extends to the MeV range. Within this energy range, the metal thickness required for gamma-ray absorption is mostly in the millimeter scale, and the corresponding distribution of the gamma-ray transmission rate is as shown in Figure 8(b). To solve the gamma-ray spectrum in this energy range, we employed an iterative fitting method based on underdetermined equations using the least-squares approach.

Based on the electron spectrum, the corresponding gamma-ray spectrum can be calculated as a reference spectrum. Within the energy range of the reference

https://doi.org/10.1017/hpl.2025.36 Published online by Cambridge University Press

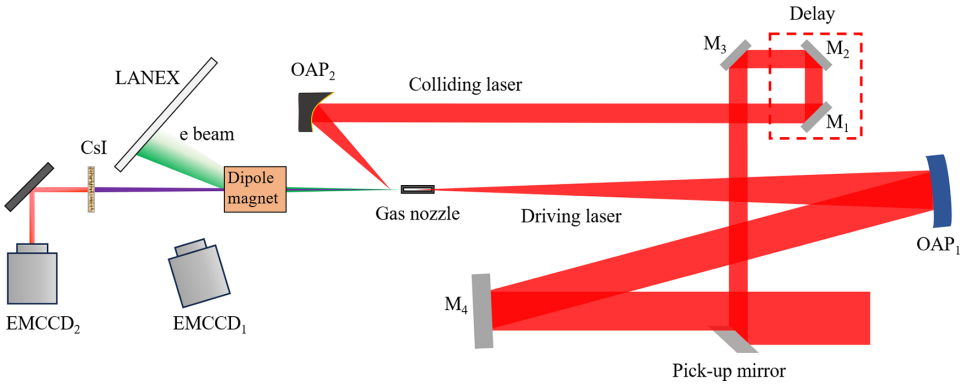


Figure 9. The overlap geometry of the experimental schematic diagram.

spectrum, the gamma-ray reference spectra are discretized by selecting evenly spaced energy reference points E_j ($j = 1, 2, 3, \ldots, n$). The number of photons corresponding to each energy point is defined as N_j. Let the number of metal filters be m ($m < n$), and use this distribution as the reference spectrum type to substitute it into the gamma-ray transmission curve T_{ij}. The gamma-ray intensity distribution $S_i = \sum_j T_{ij} N_j$ is then obtained under different thicknesses and materials. Meanwhile, the experimentally measured intensity distribution is r_i ($i = 1, 2, 3, \ldots, m$), as shown in Figure 8(a). Considering the relatively low response efficiency of the image plate to MeV gamma-rays, CsI crystals are used here to diagnose the energy deposition distribution of gamma-rays (where the response of CsI to gamma-rays of different energies is R_{ij}). For simplicity, we define $T'_{ij} = T_{ij} R_{ij}$. Following this, the evaluation function is defined as the variance between the signal intensity derived from the reference spectrum and the measured signal:

$$\sigma = \sum_i (r_i - S_i)^2. \tag{6}$$

With this evaluation function, multiple iterative calculations are performed and the iterative function is as follows[3]:

$$N'_j = N_j + \frac{\alpha \sum_i \left(T'_{ij} \times \frac{r_i - S_i}{\sum_i T'_{ik}} \right)}{\sum_i T'_{kj}}. \tag{7}$$

The iteration proceeds until the variance minimizes, at which point the process concludes, yielding the final radiation spectrum. The errors mainly arise from the numerical fluctuations in signal intensity across various regions of the experimental results.

Appendix B. The experimental schematic diagram

The primary components of the experiment include two laser beams, a gas nozzle and diagnostic systems for both electrons and radiation, as shown in Figure 9. A portion of the laser beam from the main optical path is extracted using a pick-up mirror to serve as the collision laser, while the remaining portion is focused by an $F\#$ 20 long-focus OAP mirror onto a gas nozzle. After passing through a delay line, the collision laser is focused by an $F\#$ 5 OAP mirror to a point 1 mm downstream of the nozzle. After scattering, electrons are deflected by a dipole magnet to measure the electron energy spectrum, and the emitted radiation hits a CsI scintillator to produce fluorescence, which is used to observe the profile of high-energy gamma radiation.

For energy spectrum measurements, filters are added between the magnet and CsI to perform radiation spectrum diagnostics. When the radiation energy is of the order of tens of keV or lower, an image plate is used instead of the CsI scintillator to image the radiation profile. For polarization measurements, a cylindrical plastic converter is placed after the electron deflection, along with four image plates positioned perpendicular to each other.

Acknowledgements

This work is supported by the National Key R&D Program of China (Grant No. 2021YFA1601700), the National Natural Science Foundation of China (Grant Nos. 12074251, 11991073, 12335016, 12105174 and 12225505) and the Strategic Priority Research Program of the Chinese Academy of Sciences (Grant Nos. XDA25030400 and XDA25010100). The authors would like to acknowledge the sponsorship from the Yangyang Development Fund. The authors thank Songyu Ge and Rongzhao Hu from Shanghai Run Li Vacuum Technology Co., Ltd.

References

1. J. Schwinger, Phys. Rev. **82**, 664 (1951).
2. T. Tajima and J. M. Dawson, Phys. Rev. Lett. **43**, 267 (1979).
3. K. Ta Phuoc, S. Corde, C. Thaury, V. Malka, A. Tafzi, J. P. Goddet, R. C. Shah, S. Sebban, and A. Rousse, Nat. Photonics **6**, 308 (2012).
4. H.-E. Tsai, X. Wang, J. M. Shaw, Z. Li, A. V. Arefiev, X. Zhang, R. Zgadzaj, W. Henderson, V. Khudik, G. Shvets, and M. C. Downer, Phys. Plasmas **22**, 023106 (2015).

https://doi.org/10.1017/hpl.2025.36 Published online by Cambridge University Press

5. C. Yu, R. Qi, W. Wang, J. Liu, W. Li, C. Wang, Z. Zhang, J. Liu, Z. Qin, M. Fang, K. Feng, Y. Wu, Y. Tian, Y. Xu, F. Wu, Y. Leng, X. Weng, J. Wang, F. Wei, Y. Yi, Z. Song, R. Li, and Z. Xu, Sci. Rep. **6**, 29518 (2016).
6. A. Döpp, E. Guillaume, C. Thaury, J. Gautier, I. Andriyash, A. Lifschitz, V. Malka, A. Rousse, and K. T. Phuoc, Plasma Phys. Control. Fusion **58**, 034005 (2016).
7. C. Zhu, J. Wang, J. Feng, Y. Li, D. Li, M. Li, Y. He, J. Ma, J. Tan, B. Zhang, W. Yan, and L. Chen, Plasma Phys. Control. Fusion **61**, 024001 (2019).
8. Y. Wu, C. Yu, Z. Qin, W. Wang, R. Qi, Z. Zhang, K. Feng, L. Ke, Y. Chen, C. Wang, J. Liu, R. Li, and Z. Xu, Plasma Phys. Control. Fusion **61**, 085030 (2019).
9. Y. Ma, J. Hua, D. Liu, Y. He, T. Zhang, J. Chen, F. Yang, X. Ning, H. Zhang, Y. Du, and W. Lu, Phys. Rev. Appl. **19**, 014073 (2023).
10. Y.-J. Gu and S. Weber, Opt. Express **26**, 19932 (2018).
11. J. M. Cole, K. T. Behm, E. Gerstmayr, T. G. Blackburn, J. C. Wood, C. D. Baird, M. J. Duff, C. Harvey, A. Ilderton, A. S. Joglekar, K. Krushelnick, S. Kuschel, M. Marklund, P. McKenna, C. D. Murphy, K. Poder, C. P. Ridgers, G. M. Samarin, G. Sarri, D. R. Symes, A. G. R. Thomas, J. Warwick, M. Zepf, Z. Najmudin, and S. P. D. Mangles, Phys. Rev. X **8**, 011020 (2018).
12. K. Poder, M. Tamburini, G. Sarri, A. Di Piazza, S. Kuschel, C. D. Baird, K. Behm, S. Bohlen, J. M. Cole, D. J. Corvan, M. Duff, E. Gerstmayr, C. H. Keitel, K. Krushelnick, S. P. D. Mangles, P. McKenna, C. D. Murphy, Z. Najmudin, C. P. Ridgers, G. M. Samarin, D. R. Symes, A. G. R. Thomas, J. Warwick, and M. Zepf, Phys. Rev. X **8**, 031004 (2018).
13. N. D. Powers, I. Ghebregziabher, G. Golovin, C. Liu, S. Chen, S. Banerjee, J. Zhang, and D. P. Umstadter, Nat. Photonics **8**, 28 (2014).
14. S. Chen, N. D. Powers, I. Ghebregziabher, C. M. Maharjan, C. Liu, G. Golovin, S. Banerjee, J. Zhang, N. Cunningham, A. Moorti, S. Clarke, S. Pozzi, and D. P. Umstadter, Phys. Rev. Lett. **110**, 155003 (2013).
15. C. Liu, G. Golovin, S. Chen, J. Zhang, B. Zhao, D. Haden, S. Banerjee, J. Silano, H. Karwowski, and D. Umstadter, Opt. Lett. **39**, 4132 (2014).
16. K. Khrennikov, J. Wenz, A. Buck, J. Xu, M. Heigoldt, L. Veisz, and S. Karsch, Phys. Rev. Lett. **114**, 195003 (2015).
17. W. Yan, C. Fruhling, G. Golovin, D. Haden, J. Luo, P. Zhang, B. Zhao, J. Zhang, C. Liu, M. Chen, S. Chen, S. Banerjee, and D. Umstadter, Nat. Photonics **11**, 514 (2017).
18. A. Pukhov and J. Meyer-ter Vehn, Appl. Phys. B Lasers Opt. **74**, 355 (2002).
19. L. B. Fletcher, H. J. Lee, T. Döppner, E. Galtier, B. Nagler, P. Heimann, C. Fortmann, S. LePape, T. Ma, M. Millot, A. Pak, D. Turnbull, D. A. Chapman, D. O. Gericke, J. Vorberger, T. White, G. Gregori, M. Wei, B. Barbrel, R. W. Falcone, C.-C. Kao, H. Nuhn, J. Welch, U. Zastrau, P. Neumayer, J. B. Hastings, and S. H. Glenzer, Nat. Photonics **9**, 274 (2015).
20. T. Gorkhover, S. Schorb, R. Coffee, M. Adolph, L. Foucar, D. Rupp, A. Aquila, J. D. Bozek, S. W. Epp, B. Erk, L. Gumprecht, L. Holmegaard, A. Hartmann, R. Hartmann, G. Hauser, P. Holl, A. Hömke, P. Johnsson, N. Kimmel, K.-U. Kühnel, M. Messerschmidt, C. Reich, A. Rouzée, B. Rudek, C. Schmidt, J. Schulz, H. Soltau, S. Stern, G. Weidenspointner, B. White, J. Küpper, L. Strüder, I. Schlichting, J. Ullrich, D. Rolles, A. Rudenko, T. Möller, and C. Bostedt, Nat. Photonics **10**, 93 (2016).
21. A. Schropp, R. Hoppe, V. Meier, J. Patommel, F. Seiboth, Y. Ping, D. G. Hicks, M. A. Beckwith, G. W. Collins, A. Higginbotham, J. S. Wark, H. J. Lee, B. Nagler, E. C. Galtier, B. Arnold, U. Zastrau, J. B. Hastings, and C. G. Schroer, Sci. Rep. **5**, 11089 (2015).
22. T. Kluge, C. Rödel, M. Rödel, A. Pelka, E. E. McBride, L. B. Fletcher, M. Harmand, A. Krygier, A. Higginbotham, M. Bussmann, E. Galtier, E. Gamboa, A. L. Garcia, M. Garten, S. H. Glenzer, E. Granados, C. Gutt, H. J. Lee, B. Nagler, W. Schumaker, F. Tavella, M. Zacharias, U. Schramm, and T. E. Cowan, Phys. Plasmas **24**, 102709 (2017).
23. T. Kluge, M. Rödel, J. Metzkes-Ng, A. Pelka, A. L. Garcia, I. Prencipe, M. Rehwald, M. Nakatsutsumi, E. E. McBride, T. Schönherr, M. Garten, N. J. Hartley, M. Zacharias, J. Grenzer, A. Erbe, Y. M. Georgiev, E. Galtier, I. Nam, H. J. Lee, S. Glenzer, M. Bussmann, C. Gutt, K. Zeil, C. Rödel, U. Hübner, U. Schramm, and T. E. Cowan, Phys. Rev. X **8**, 031068 (2018).
24. M. Mo, S. Murphy, Z. Chen, P. Fossati, R. Li, Y. Wang, X. Wang, and S. Glenzer, Sci. Adv. **5**, eaaw0392 (2019).
25. L. Gaus, L. Bischoff, M. Bussmann, E. Cunningham, C. B. Curry, J. E, E. Galtier, M. Gauthier, A. L. García, M. Garten, S. Glenzer, J. Grenzer, C. Gutt, N. J. Hartley, L. Huang, U. Hübner, D. Kraus, H. J. Lee, E. E. McBride, J. Metzkes-Ng, B. Nagler, M. Nakatsutsumi, J. Nikl, M. Ota, A. Pelka, I. Prencipe, L. Randolph, M. Rödel, Y. Sakawa, H.-P. Schlenvoigt, M. Šmíd, F. Treffert, K. Voigt, K. Zeil, T. E. Cowan, U. Schramm, and T. Kluge, Phys. Rev. Res. **3**, 043194 (2021).
26. Y. Wu, S. Wang, B. Zhu, Y. Yan, M. Yu, G. Li, X. Zhang, Y. Yang, F. Tan, F. Lu, B. Bi, X. Mao, Z. Wang, Z. Zhao, J. Su, W. Zhou, and Y. Gu, Matter Radiat. Extremes **9**, 037202 (2024).
27. D. Habs, T. Tajima, J. Schreiber, C. P. J. Barty, M. Fujiwara, and P. G. Thirolf, Eur. Phys. J. D **55**, 279 (2009).
28. H. A. Weidenmüller, Phys. Rev. Lett. **106**, 122502 (2011).
29. G. Breit and J. A. Wheeler, Phys. Rev. **46**, 1087 (1934).
30. H. R. Reiss, J. Math. Phys. **3**, 59 (1962).
31. Y.-J. Gu, O. Klimo, S. V. Bulanov, and S. Weber, Commun. Phys. **1**, 93 (2018).
32. V. Petrillo, G. Dattoli, I. Drebot, and F. Nguyen, Phys. Rev. Lett. **117**, 123903 (2016).
33. Y.-Y. Chen, J.-X. Li, K. Z. Hatsagortsyan, and C. H. Keitel, Phys. Rev. Lett. **121**, 074801 (2018).
34. M. Ababekri, R.-T. Guo, F. Wan, B. Qiao, Z. Li, C. Lv, B. Zhang, W. Zhou, Y. Gu, and J.-X. Li, Phys. Rev. D **109**, 016005 (2024).
35. A. Döpp, K. T. Phuoc, and I. A. Andriyash, J. Plasma Phys. **89**, 965890501 (2023).
36. W. Zhou, W. Yan, J. Wang, and L. Chen, Ultrafast Sci. **3**, 0005 (2023).
37. A. Debus, S. Bock, M. Bussmann, T. E. Cowan, A. Jochmann, T. Kluge, S. D. Kraft, R. Sauerbrey, K. Zeil, and U. Schramm, Proc. SPIE **7359**, 735908 (2009).
38. J. Wenz, A. Döpp, K. Khrennikov, S. Schindler, M. F. Gilljohann, H. Ding, J. Götzfried, A. Buck, J. Xu, M. Heigoldt, W. Helml, L. Veisz, and S. Karsch, Nat. Photonics **13**, 263 (2019).
39. P.-H. Huang, K. R. Kase, and B. E. Bjärngard, Med. Phys. **9**, 695 (1982).
40. H. Ohsumi and T.-h. Arima, Adv. Phys. X **1**, 128 (2016).
41. Y. Togawa, Y. Kousaka, K. Inoue, and J.-i. Kishine, J. Phys. Soc. Jpn. **85**, 112001 (2016).
42. S. L. Zhang, G. Van Der Laan, and T. Hesjedal, Phys. Rev. B **96**, 094401 (2017).
43. A. T. Schmitt, Y. Joly, K. S. Schulze, B. Marx-Glowna, I. Uschmann, B. Grabiger, H. Bernhardt, R. Loetzsch, A. Juhin, J. Debray, H.-C. Wille, H. Yavaş, G. G. Paulus, and R. Röhlsberger, Optica **8**, 56 (2021).
44. D. P. Siddons, M. Hart, Y. Amemiya, and J. B. Hastings, Phys. Rev. Lett. **64**, 1967 (1990).
45. G.-P. An, Y.-L. Chi, Y.-L. Dang, G.-Y. Fu, B. Guo, Y.-S. Huang, C.-Y. He, X.-C. Kong, X.-F. Lan, J.-C. Li, F.-L. Liu, J.-S. Shi, X.-J. Sun, Y. Wang, J.-L. Wang, L. Wang, Y.-Y. Wei,

https://doi.org/10.1017/hpl.2025.36 Published online by Cambridge University Press

G. Wu, G.-L. Xu, X.-F. Xi, G.-J. Yang, C.-L. Zhang, Z. Zhang, Z.-P. Zheng, X.-D. Zhang, and S.-P. Zhang, Matter Radiat. Extremes **3**, 219 (2018).
46. G. O. Depaola, Nucl. Instrum. Methods Phys. Res. Sect. A **512**, 619 (2003).
47. O. Lundh, J. Lim, C. Rechatin, L. Ammoura, A. Ben-Ismaïl, X. Davoine, G. Gallot, J.-P. Goddet, E. Lefebvre, V. Malka, and J. Faure, Nat. Phys. **7**, 219 (2011).
48. D. Y. Kim, C. I. Hojbota, M. Mirzaie, S. K. Lee, K. Y. Kim, J. H. Sung, and C. H. Nam, Rev. Sci. Instrum. **93**, 113001 (2022).
49. D. J. Corvan, T. Dzelzainis, C. Hyland, G. Nersisyan, M. Yeung, M. Zepf, and G. Sarri, Opt. Express **24**, 3127 (2016).
50. A. Gonoskov, T. G. Blackburn, M. Marklund, and S. S. Bulanov, Rev. Mod. Phys. **94**, 045001 (2022).
51. A. Di Piazza, C. Müller, K. Z. Hatsagortsyan, and C. H. Keitel, Rev. Mod. Phys. **84**, 1177 (2012).
52. S. Weber, S. Bechet, S. Borneis, L. Brabec, M. Bučka, E. Chacon-Golcher, M. Ciappina, M. DeMarco, A. Fajstavr, K. Falk, E.-R. Garcia, J. Grosz, Y.-J. Gu, J.-C. Hernandez, M. Holec, P. Janečka, M. Jantač, M. Jirka, H. Kadlecova, D. Khikhlukha, O. Klimo, G. Korn, D. Kramer, D. Kumar, T. Lastovička, P. Lutoslawski, L. Morejon, V. Olšovcová, M. Rajdl, O. Renner, B. Rus, S. Singh, M. Šmid, M. Sokol, R. Versaci, R. Vrána, M. Vranic, J. Vyskočil, A. Wolf, and Q. Yu, Matter Radiat. Extremes **2**, 149 (2017).
53. Y.-J. Gu, M. Jirka, O. Klimo, and S. Weber, Matter Radiat. Extremes **4**, 064403 (2019).
54. A. S. Samsonov, E. N. Nerush, and I. Yu. Kostyukov, Matter Radiat. Extremes **8**, 014402 (2023).
55. S. S. Bulanov, C. B. Schroeder, E. Esarey, and W. P. Leemans, Phys. Rev. A **87**, 062110 (2013).
56. T. Heinzl, B. King, and A. J. MacLeod, Phys. Rev. A **102**, 063110 (2020).
57. A. Di Piazza, M. Tamburini, S. Meuren, and C. H. Keitel, Phys. Rev. A **99**, 022125 (2019).
58. M. Kh. Khokonov and H. Nitta, Phys. Rev. Lett. **89**, 094801 (2002).
59. A. Ilderton, B. King, and D. Seipt, Phys. Rev. A **99**, 042121 (2019).
60. T. Podszus and A. Di Piazza, Phys. Rev. D **99**, 076004 (2019).
61. E. G. Gelfer, A. M. Fedotov, A. A. Mironov, and S. Weber, Phys. Rev. D **106**, 056013 (2022).
62. W. Li, Z. Gan, L. Yu, C. Wang, Y. Liu, Z. Guo, L. Xu, M. Xu, Y. Hang, Y. Xu, J. Wang, P. Huang, H. Cao, B. Yao, X. Zhang, L. Chen, Y. Tang, S. Li, X. Liu, S. Li, M. He, D. Yin, X. Liang, Y. Leng, R. Li, and Z. Xu, Opt. Lett. **43**, 5681 (2018).
63. E. Cartlidge, Science **359**, 382 (2018).
64. K. Burdonov, A. Fazzini, V. Lelasseux, J. Albrecht, P. Antici, Y. Ayoul, A. Beluze, D. Cavanna, T. Ceccotti, M. Chabanis, A. Chaleil, S. N. Chen, Z. Chen, F. Consoli, M. Cuciuc, X. Davoine, J. P. Delaneau, E. d'Humières, J.-L. Dubois, C. Evrard, E. Filippov, A. Freneaux, P. Forestier-Colleoni, L. Gremillet, V. Horny, L. Lancia, L. Lecherbourg, N. Lebas, A. Leblanc, W. Ma, L. Martin, F. Negoita, J.-L. Paillard, D. Papadopoulos, F. Perez, S. Pikuz, G. Qi, F. Quéré, L. Ranc, P.-A. Söderström, M. Scisciò, S. Sun, S. Vallières, P. Wang, W. Yao, F. Mathieu, P. Audebert, and J. Fuchs, Matter Radiat. Extremes **6**, 064402 (2021).
65. M. Aléonard, M. Altarelli, P. Antici, A. Apolonskiy, P. Audebert, A. Bartnik, C. Barty, A. Bernstein, J. Biegert, P. Böni, N. Booth, D. Bote, S. Bulanov, R. Butkus, L. Cardoso, J. P. Chambaret, D. Charambilidis, G. Cheriaux, R. Clarke, and M. Zepf, *WHITEBOOK ELI – Extreme Light Infrastructure; Science and Technology with Ultra-Intense Lasers* (Andreas Thoss, 2011).
66. C. Radier, O. Chalus, M. Charbonneau, S. Thambirajah, G. Deschamps, S. David, J. Barbe, E. Etter, G. Matras, S. Ricaud, V. Leroux, C. Richard, F. Lureau, A. Baleanu, R. Banici, A. Gradinariu, C. Caldararu, C. Capiteanu, A. Naziru, B. Diaconescu, V. Iancu, R. Dabu, D. Ursescu, I. Dancus, C. A. Ur, K. A. Tanaka, and N. V. Zamfir, High Power Laser Sci. Eng. **10**, e21 (2022).
67. J. D. Zuegel, S.-W. Bahk, I. A. Begishev, J. Bromage, C. Dorrer, A. V. Okishev, and J. B. Oliver. In *CLEO: 2014* (OSA, 2014), paper JTh4L.4.
68. V. I. Ritus, J. Sov. Laser Res. **6**, 497 (1985).
69. A. Di Piazza, K. Z. Hatsagortsyan, and C. H. Keitel, Phys. Rev. Lett. **105**, 220403 (2010).
70. A. Di Piazza, Lett. Math. Phys. **83**, 305 (2008).
71. C. Bula, K. T. McDonald, E. J. Prebys, C. Bamber, S. Boege, T. Kotseroglou, A. C. Melissinos, D. D. Meyerhofer, W. Ragg, D. L. Burke, R. C. Field, G. Horton-Smith, A. C. Odian, J. E. Spencer, D. Walz, S. C. Berridge, W. M. Bugg, K. Shmakov, and A. W. Weidemann, Phys. Rev. Lett. **76**, 3116 (1996).
72. D. L. Burke, R. C. Field, G. Horton-Smith, J. E. Spencer, D. Walz, S. C. Berridge, W. M. Bugg, K. Shmakov, A. W. Weidemann, C. Bula, K. T. McDonald, E. J. Prebys, C. Bamber, S. J. Boege, T. Koffas, T. Kotseroglou, A. C. Melissinos, D. D. Meyerhofer, D. A. Reis, and W. Ragg, Phys. Rev. Lett. **79**, 1626 (1997).
73. H. Schwoerer, B. Liesfeld, H.-P. Schlenvoigt, K.-U. Amthor, and R. Sauerbrey, Phys. Rev. Lett. **96**, 014802 (2006).
74. G. Sarri, D. J. Corvan, W. Schumaker, J. M. Cole, A. Di Piazza, H. Ahmed, C. Harvey, C. H. Keitel, K. Krushelnick, S. P. D. Mangles, Z. Najmudin, D. Symes, A. G. R. Thomas, M. Yeung, Z. Zhao, and M. Zepf, Phys. Rev. Lett. **113**, 224801 (2014).
75. M. Mirzaie, C. I. Hojbota, D. Y. Kim, V. B. Pathak, T. G. Pak, C. M. Kim, H. W. Lee, J. W. Yoon, S. K. Lee, Y. J. Rhee, M. Vranic, Ó. Amaro, K. Y. Kim, J. H. Sung, and C. H. Nam, Nat. Photonics **18**, 1212 (2024).
76. I. C. E. Turcu, F. Negoita, D. A. Jaroszynski, P. Mckenna, S. Balascuta, D. Ursescu, I. Dancus, M. O. Cernaianu, M. V. Tataru, P. Ghenuche, D. Stutman, A. Boianu, M. Risca, M. Toma, C. Petcu, G. Acbas, S. R. Yoffe, A. Noble, B. Ersfeld, E. Brunetti, R. Capdessus, C. Murphy, C. P. Ridgers, D. Neely, S. P. D. Mangles, R. J. Gray, A. G. R. Thomas, J. G. Kirk, A. Ilderton, M. Marklund, D. F. Gordon, B. Hafizi, D. Kaganovich, J. P. Palastro, E. D'Humieres, M. Zepf, G. Sarri, H. Gies, F. Karbstein, J. Schreiber, G. G. Paulus, B. Dromey, C. Harvey, A. Di Piazza, C. H. Keitel, M. C. Kaluza, S. Gales, and N. V. Zamfir, Rom. Rep. Phys. **68**, S145 (2016).
77. Z. Chen, S. Meuren, E. Gerstmayr, V. Yakimenko, P. H. Bucksbaum, D. A. Reis, and The E-320 Collaboration, in *Optica High-brightness Sources and Light-driven Interactions Congress 2022* (Optica Publishing Group, 2022), paper HF4B.6.
78. LUXE Collaboration, H. Abramowicz, M. A. Soto, M. Altarelli, R. Aßmann, A. Athanassiadis, G. Avoni, T. Behnke, M. Benettoni, Y. Benhammou, J. Bhatt, T. Blackburn, C. Blanch, S. Bonaldo, S. Boogert, O. Borysov, M. Borysova, V. Boudry, D. Breton, R. Brinkmann, M. Bruschi, F. Burkart, K. Büßer, N. Cavanagh, F. Dal Corso, W. Decking, M. Deniaud, O. Diner, U. Dosselli, M. Elad, L. Epshteyn, D. Esperante, T. Ferber, M. Firlej, T. Fiutowski, K. Fleck, N. Fuster-Martinez, K. Gadow, F. Gaede, A. Gallas, H. G. Cabrera, E. Gerstmayr, V. Ghenescu, M. Giorato, N. Golubeva, C. Grojean, P. Grutta, G. Grzelak, J. Hallford, L. Hartman, B. Heinemann, T. Heinzl, L. Helary, L. Hendriks, M. Hoffmann, D. Horn, S. Huang, X. Huang, M. Idzik, A. Irles, R. Jacobs, B. King, M. Klute, A. Kropf, E. Kroupp, H. Lahno, F. L. Manghi, J. Lawhorn, A. Levanon, A. Levi, L. Levinson, A. Levy, I. Levy, A. Liberman, B. Liss, B. List, J. List, W. Lohmann, J. Maalmi, T. Madlener, V. Malka, T. Marsault, S. Mattiazzo, F. Meloni, D. Miron,

https://doi.org/10.1017/hpl.2025.36 Published online by Cambridge University Press

M. Morandin, J. Moroń, J. Nanni, A. T. Neagu, E. Negodin, A. Paccagnella, D. Pantano, D. Pietruch, I. Pomerantz, R. Pöschl, P. M. Potlog, R. Prasad, R. Quishpe, E. Ranken, A. Ringwald, A. Roich, F. Salgado, A. Santra, G. Sarri, A. Sävert, A. Sbrizzi, S. Schmitt, I. Schulthess, S. Schuwalow, D. Seipt, G. Simi, Y. Soreq, D. Spataro, M. Streeter, K. Swientek, N. T. Hod, T. Teter, A. Thiebault, D. Thoden, N. Trevisani, R. Urmanov, S. Vasiukov, S. Walker, M. Warren, M. Wing, Y. C. Yap, N. Zadok, M. Zanetti, A. F. Żarnecki, P. Zbińkowski, K. Zembaczyński, M. Zepf, D. Zerwas, W. Ziegler, and M. Zuffa, Eur. Phys. J. Spec. Top. **233**, 1709 (2024).

79. E. E. Los, E. Gerstmayr, C. Arran, M. J. V. Streeter, C. Colgan, C. C. Cobo, B. Kettle, T. G. Blackburn, N. Bourgeois, L. Calvin, J. Carderelli, N. Cavanagh, S. J. D. Dann, A. Di Piazza, R. Fitzgarrald, A. Ilderton, C. H. Keitel, M. Marklund, P. McKenna, C. D. Murphy, Z. Najmudin, P. Parsons, P. P. Rajeev, D. R. Symes, M. Tamburini, A. G. R. Thomas, J. C. Wood, M. Zepf, G. Sarri, C. P. Ridgers, and S. P. D. Mangles, arXiv:2407.12071 (2024).
80. A. Matheron, J.-R. Marquès, V. Lelasseux, Y. Shou, I. A. Andriyash, V. L. J. Phung, Y. Ayoul, A. Beluze, I. Dăncuş, F. Dorchies, F. D'Souza, M. Dumergue, M. Frotin, J. Gautier, F. Gobert, M. Gugiu, S. Krishnamurthy, I. Kargapolov, E. Kroupp, L. Lancia, A. Lazăr, A. Leblanc, M. Lo, D. Mataja, F. Mathieu, D. Papadopoulos, P. S. M. Claveria, K. T. Phuoc, A.-M. Talposi, S. Tata, C. A. Ur, D. Ursescu, L. Văsescu, D. Doria, V. Malka, P. Ghenuche, and S. Corde, arXiv:2412.19337 (2024).
81. I. V. Khutoretsky, Rev. Sci. Instrum. **66**, 773 (1995).
82. T. Bonnet, M. Comet, D. Denis-Petit, F. Gobet, F. Hannachi, M. Tarisien, M. Versteegen, and M. M. Aléonard, Rev. Sci. Instrum. **84**, 103510 (2013).

https://doi.org/10.1017/hpl.2025.36 Published online by Cambridge University Press